International Journal of Heat and Mass Transfer 150 (2020) 119308

Contents lists available at ScienceDirect

International Journal of Heat and Mass Transfer

journal homepage: www.elsevier.com/locate/hmt

A DEM modeling of biomass fast pyrolysis in a double auger reactor

Fenglei Qi [a,*], Mark Mba Wright [b]

[a] FSTC, University of Luxembourg, 2, avenue de l'Université, 4365 Esch-sur-Alzette, Luxembourg
[b] Department of Mechanical Engineering, Iowa State University, Ames, IA, 50010 USA

ARTICLE INFO

Article history:
Received 16 September 2019
Revised 29 November 2019
Accepted 2 January 2020

Keywords:
Fast pyrolysis
Discrete Element Method
Auger reactor
Reacting granular flow
Scalibility

ABSTRACT

Thermochemical conversion of biomass via fast pyrolysis is a proven pathway to product low-carbon crude bio-oils. In this research, an extended discrete element method (DEM) is proposed for simulating biomass fast pyrolysis reacting granular flows in a double auger reactor, in which particle hydrodynamics and interparticle heat transfer processes are involved and coupled with chemical reactions in solid particles. An adaptive time step algorithm is proposed to achieve a stable coupling between the integration of reaction ordinary differential equations and the DEM solver, and the algorithm is proven computationally efficient. A multi-component fast pyrolysis kinetics is adopted and its modeling accuracy is assessed by carrying out simulations of benchmark biomass pyrolysis experiments and comparing the prediction results with experimental data. The predicted product yields of bio-oil, char and non-condensable gas from the simulation of the biomass fast pyrolysis in the auger reactor are in satisfactory agreement with experimental measurements. The decomposition rates of biomass components in the reactor are revealed from the simulation and the pyrolysis number Py is calculated from the decomposition rate of biomass and the heat transfer coefficient. The Py number illustrates that the biomass fast pyrolysis process is limited by the heat transfer process at particle size of 2 mm.

1. Introduction

Biomass is an abundant renewable resource that is widely produced through photosynthesis in various plants. In recent decades, efficient utilization of the biomass resource via thermochemical conversion such as gasification and fast pyrolysis has been promoted to reduce human carbon footprint [1–5]. Biomass fast pyrolysis is a process targeting production of crude bio-oil with two side products of non-condensable gas and char, which is illustrated in Fig. 1. The crude bio-oil can be upgraded into low-carbon chemicals and fuels in a downstream processing. The yields of bio-oil, char and non-condensable gas are usually subject to changes of feedstock type, reactor temperature and heat and mass transport process in fast pyrolysis reactors. Maximizing the bio-oil yield requires a good understanding of the adopted reactor and its intrinsic heat and mass transport process.

Different reactor configurations have been studied for thermochemical conversion of biomass. Circulating fluidized beds (CFB), bubbling fluidized beds and auger reactors are among the commonly used reactors in previous research [3,6,7]. In an auger reactor, mechanical forces are provided to the bed to enhance particle mixing and simultaneously achieve particulate matter transport for continuous operation. Heat carrier particles could be fed into the reactor to provide heat source for biomass particles. Some experimental studies have shown that auger reactor systems have similar bio-oil yield performance compared with bubbling fluidized bed reactor systems [8,9]. The pyrolysis process in an auger reactor configuration is a reactive granular flow system which involves particle flow, heat transfer and biomass thermochemical conversion reactions at the same time. Probing the physical transport phenomena and the interplay between the physical transport phenomena and chemical reactions is essential for reactor design and optimization. While there are still a lot of challenges in experimentally measuring flow information in granular flows, the installment of internal structures in the auger reactor makes it even harder to probe local granular flow information. Numerical simulation, as an alternative way, is capable of predicting granular flow and heat transfer behaviors in the reactor and providing useful information such as particle residence time, particle mixing degree, and heat transfer coefficient [10,11] for reactor diagnosis.

Computational Fluid Dynamics (CFD) simulation allows for evaluating reactor-scale heat and mass transport effects on the biomass thermochemical conversion process. Eulerian-Eulerian and Eulerian-Lagrangian approaches are among the most advanced and popular methods for modeling reactive particulate systems as re-

* Corresponding author.
E-mail addresses: fenglei.qi@outlook.com (F. Qi), markmw@iastate.edu (M.M. Wright).

https://doi.org/10.1016/j.ijheatmasstransfer.2020.119308
0017-9310/

Nomenclature

A_r	reaction frequency factor, 1/s
c	contact radius correction coefficient
c_p	specific heat capacity, J/kg · K
d_{ij}	distance between particle centers
d_p	particle diameter, m
D	auger flight diameter, m
e	coefficient of restitution
E_i	Young's modulus, Pa
E_r	activation energy, J/mol
E^*	equivalent Young's modulus, Pa
f	volumetric fill level
F_{ij}	view factor between surfaces
$\boldsymbol{F}_i^f$	drag force acting on particle i, N
$\boldsymbol{F}_i^g$	gravitational force acting on particle i, N
$\boldsymbol{F}_{ij}^c$	particle collision force, N
$\boldsymbol{F}_{n,ij}^c$	normal collision force, N
$\boldsymbol{F}_{t,ij}^c$	tangential collision force, N
G_i	particle shear modulus, Pa
G^*	equivalent shear modulus, Pa
h	heat transfer coefficient, W/m^2 · K
m_{vi}^p	vapor species mass in the particle, kg
m_{water}^p	moisture mass in the particle, kg
m^*	particle equivalent mass, kg
$\hat{\boldsymbol{n}}_{ij}$	unit vector in the normal direction
P	auger pitch length, m
Py	pyrolysis number
Q_{ij}^{cond}	conductive heat transfer rate, J/s
Q_{ij}^{conv}	convective heat transfer rate, J/s
Q_{ij}^{pfp}	heat transfer rate by particle-fluid-particle pathway, J/s
Q_{ij}^{pp}	heat transfer rate by particle-particle pathway, J/s
Q_{ij}^{rad}	heat transfer rate by radiation pathway, J/s
R_g	gas constant, J/mol · K
R_i	radius of particle, m
R^*	particle equivalent radius
$\dot{r}_{li}$	liquid species production rate, kg/s
$\dot{r}_{gas}$	non-condensable gas production rate, kg/s
$\dot{r}_{si}$	solid species production rate, kg/s
$\dot{r}_{tar}$	tar vapor production rate, kg/s
$\dot{r}_{vi}$	vapor species production rate, kg/s
r_c	contact surface radius, m
H	gap between particles, m
I_i	particle moment of inertia, kg · m^2
k_f	fluid thermal conductivity, W/m · K
k_p	particle thermal conductivity, W/m · K
k_w	reactor wall thermal conductivity, W/m · K
L	auger mixing length, m
m_i	particle mass, kg
m_{li}^p	liquid species mass in the particle, kg
m_{si}^p	solid species mass in the particle, kg
T_i	particle temperature, K
$\boldsymbol{T}_{r,ij}$	rolling friction torque, N · m
$\boldsymbol{T}_{t,ij}$	tangential torque, N · m
$\hat{\boldsymbol{t}}_{ij}$	unit vector in tangential direction
$\boldsymbol{v}_i$	particle velocity, m/s
$\boldsymbol{v}_{rel}$	particle relative velocity, m/s
$\boldsymbol{v}_{n,rel}$	relative velocity in the normal direction, m/s
$\boldsymbol{v}_{t,rel}$	relative velocity in the tangential direction, m/s
X	biomass conversion

Greek symbols

α_s	solid fraction
β	damping coefficient
δ_n	particle overlap in the normal direction, m
δ_t	particle overlap in the tangential direction, m
ΔH	heat of reaction, J/kg
ϵ_r	radiation emissivity
μ	friction coefficient
μ_r	rolling friction coefficient
ν	Poisson's ratio
σ	Stephan-Boltzmann constant, W/m^2 · K^4
$\tau_{reaction}$	reaction time scale, s
τ_{heat}	external heat transfer time scale, s
$\boldsymbol{\omega}_i$	particle rotation velocity, rad/s
ω	auger rotating velocity, rad/s

Subscripts

b	biomass particles
l	liquid
p	particle
r	reaction or radiation
s	solid
v	vapor

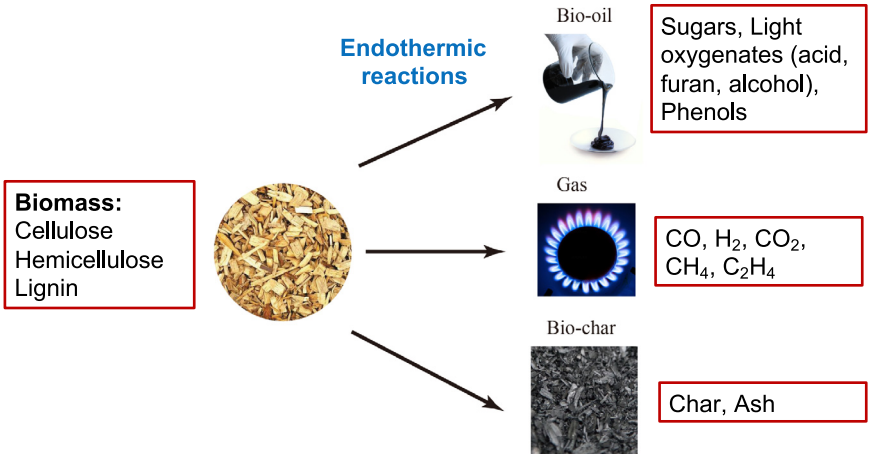

Fig. 1. A schematic description of biomass fast prolysis.

viewed in [12–14]. Eulerian-Eulerian approaches were developed in [15–21] for biomass gasification and fast pyrolysis modeling in fluidized beds. In this approach, both gaseous and solid phases are considered as continua. Separate transport equations are developed for each particle phase, which has the same mechanical and thermochemical properties. Momentum, heat and mass exchanges between two phases are properly accounted for by interaction models. Xue et al. [17,22] and Sharma et al. [18] simulated biomass fast pyrolysis in a same two-dimensional (2D) fluidized bed reactor system with MFIX software from the National Energy Technology Laboratory (NETL) and ANSYS FLUENT version 14, separately. Comparing with the experimental results, both simulations could satisfactorily predict tar yields although simplified biomass pyrolysis kinetics were adopted in their research. CFD simulations of auger reactors were also successfully carried out in [23,24] and the biomass conversion process were reasonably predicted. Eulerian-Eulerian approach is one affordable modeling approach which could perform simulations at the pilot or industrial scale but this method becomes challenging when a description of particle size distribution or multiply particle types is necessary [12].

Modeling of particle phase by Discrete Element Method (DEM) could naturally overcome the difficulties met in the Eulerian-Eulerian approach since the dynamic and thermochemical properties of each single particle are numerically solved separately and the averaging concept is avoided in this approach. Representative research could be found in [25–33]. Despite the merits mentioned earlier, some limitations of the approach are noticed in the literature which requires further development. First, the interparticle heat transfer models are not well developed and validated. For example, in the Eulerian-Lagrangian simulation of wood gasification in a fluidized bed, Gerber and Oevermann [27] suggest that the discrepancy of the predicted reactor temperature from the experimentally measured data might result from neglecting the interparticle radiative heat transfer in the simulation. Second, simulations are often carried out with limited amount of particles [27,30,33] or for short simulation time [28], which prevents the approach from applying to real operational conditions even for pilot-scale simulations. A recent study by Yang et al. [32] has managed to simulate approximately 250,000 sand particles in a three-dimensional (3D) simulation of a fluidized bed gasifier for 20 s physical time. A careful examination of the scalability of the developed approach and algorithm is necessary for modeling real-size systems with parallel computing techniques. In our research, we aim to develop a generalized DEM approach which implements well-validated heat transfer models and has a good scalability performance. Moreover, a novel adaptive time step algorithm is implemented to achieve efficient and stable coupling of particle dynamics simulation and kinetic reaction integration.

The following first describes the simulated auger reactor system and presents the developed DEM approach for biomass fast pyrolysis simulation. Next, the simulation predictions are to be compared with experimental results for validation. Thereafter, the simulation results are presented and conclusion is given at the last part showing the main findings in this research.

2. Reactor system and model description

2.1. Double auger reactor

Fig. 2 illustrates the geometry of the double auger reactor system, which has the same dimension as used in the experimental study by Brown and Brown [34]. The mixing and continuous transportation of solid particles is facilitated by the rotating augers in the trough. As shown in Fig. 2 (a), the left auger rotates in the clockwise direction while the right auger rotates in the counter-clockwise direction, which design is found to have an overall better performance [35]. Biomass particles (red oak) is fed into the reactor at inlet 1 and sand particles fed at inlet 2 are used as the heat carrier, which is proven to improve the heat transfer coefficient in the reactor [11]. The biomass particle has a particle size range of 300–710 μm in the experiments and is fed into the system at the ambient temperature. The sand particle either has a particle range of 250–600 μm (fine sand) or 600–1000 μm (coarse sand) in the experiments and is fed into the system at high temperature depending on the reaction temperature requirement. The auger rotation speed varied from 20 RPM to 60 RPM in the operation of the reactor [34].

Multiple physical phenomena are observed in the reactor system including particle mixing and heat transfer. Moreover, the biomass undergoes pyrolysis reactions as the system reaches fast pyrolysis condition. In the experiments [8,34], vacuum pressure is applied at the exit of the reactor to quickly extract vapor products and effectively prevent the secondary cracking reactions in gas phase. Since the transport of the vapor products has trivial influences on the primary decomposition reactions in the solid biomass particles, the vapor products are assumed to leave the reactors immediately after production in this research and no computational models are applied to simulate the vapor transport process in the reactor. Therefore, this research focuses on the simulation of the biomass primary decomposition reactions. The influences of the secondary cracking reactions in the gas phase can be investigated by adding a CFD model for the gas phase in future study.

2.2. Extended DEM approach for biomass thermochemical conversion

The extended DEM approach is capable of resolving particle dynamics, interparticle conductive and radiative heat transfer, and particle thermochemical conversion reactions, which enables modeling of reactive granular flows with this approach.

2.2.1. Particle dynamics

The particle dynamics is modeled by the traditional DEM approach. When two spherical particles collide, the particles are deformable at the collision point. Contact models such as the linear spring-dashpot model and the Hertz–Mindlin nonlinear model [36] are accountable for modeling the collision physics. Subsequently the contact forces are calculated from the local deformation and particle collision history. Particle displacement and velocities are updated by numerically integrating Newton's and Euler's equations for a spherical shape particle, written as

$$m_i \frac{d\boldsymbol{v}_i}{dt} = \sum_j \boldsymbol{F}_{ij}^c + \boldsymbol{F}_i^f + \boldsymbol{F}_i^g, \tag{1}$$

$$I_i \frac{d\boldsymbol{w}_i}{dt} = \sum_j \left(\boldsymbol{T}_{t,ij} + \boldsymbol{T}_{r,ij}\right), \tag{2}$$

where, m_i and I_i ($=2/5 m_i R_i^2$) are mass of particle i and moment of inertia of the particle, respectively. $\boldsymbol{v}_i$ and $\boldsymbol{w}_i$ are translational and rotational velocities of the particle. The forces in Eq. (1) include the contact force $\boldsymbol{F}_{ij}^c$ between particle i and surrounding particle j that collides with particle i, drag force acting on particle i by a fluid $\boldsymbol{F}_i^f$, and the gravitational force $\boldsymbol{F}_i^g$. The torques acting on particle i includes both $\boldsymbol{T}_{t,ij}$ and $\boldsymbol{T}_{r,ij}$. Torque $\boldsymbol{T}_{t,ij}$ is generated by the tangential force $\boldsymbol{F}_{t,ij}^c$ which is the component of the contact force $\boldsymbol{F}_{ij}^c$ with direction parallel to the contacting surface between particle i and j. Torque $\boldsymbol{T}_{r,ij}$, called rolling friction torque, is generated by the asymmetric distribution of the normal contact force $\boldsymbol{F}_{n,ij}^c$, the other component of $\boldsymbol{F}_{ij}^c$ with direction perpendicular to the contact surface. In this research, the drag force is ignored in the bed

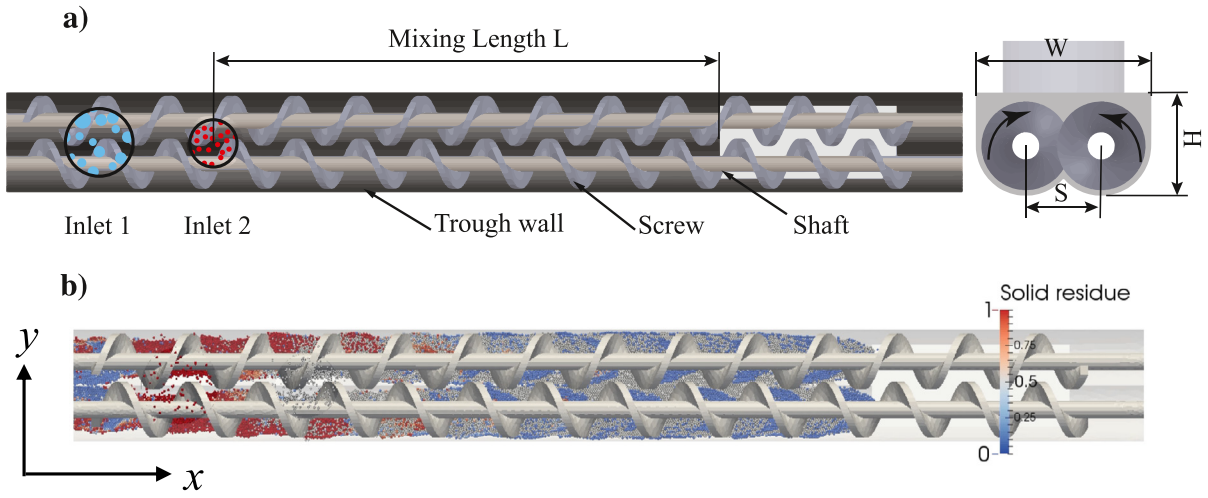

Fig. 2. (a) Geometry of the double auger reactor and (b) Biomass solid residue prediction. Biomass particles are fed into the reactor at inlet 1 and sand particles are fed into the reactor at inlet 2. The ratio of the length L to the auger flight diameter D is 10. The ratio of the auger pitch P to the auger flight diameter D is 1.25. Both biomass and sand sizes in (b) are 2 mm and the augers rotate at the speed of 40 RPM.

Table 1
Models for calculating contact forces and torques in DEM.

Force or torque	Equation
Normal force $\boldsymbol{F}^c_{n,ij}$	$\frac{4}{3}E^*\sqrt{R^*}\delta_n^{3/2}\hat{\boldsymbol{n}}_{ij} - \sqrt{\frac{20}{3}}\beta\left(m^*E^*\sqrt{R^*\delta_n}\right)^{1/2}\boldsymbol{v}_{n,rel}$
Tangential force $\boldsymbol{F}^c_{t,ij}$	$-8G^*\sqrt{R^*\delta_n}\int\delta_t\hat{\boldsymbol{t}}_{ij} - \sqrt{\frac{20}{3}}\beta\left(4m^*G^*\sqrt{R^*\delta_n}\right)^{1/2}\boldsymbol{v}_{t,rel}$
Torque $\boldsymbol{T}_{t,ij}$	$\boldsymbol{R}_i \times \boldsymbol{F}^c_{t,ij}$
Torque $\boldsymbol{T}_{r,ij}$	$-\frac{4}{3}\mu_r E^* R^* \sqrt{R^*}\delta_n^{3/2}\boldsymbol{\omega}_{rel}/\lvert\boldsymbol{\omega}_{rel}\rvert$

where, $\frac{1}{m*} = \frac{1}{m_i} + \frac{1}{m_j}$, $\frac{1}{R*} = \frac{1}{R_i} + \frac{1}{R_j}$, $\frac{1}{E*} = \frac{(1-\nu_i^2)}{E_i} + \frac{(1-\nu_j^2)}{E_j}$ $\frac{1}{G*} = \frac{2(2-\nu_i)(1+\nu_i)}{G_i} + \frac{2(2-\nu_j)(1+\nu_j)}{G_j}$, $\beta = \ln(e)/\sqrt{\ln^2(e)+\pi^2}$ $\hat{\boldsymbol{n}}_{ij} = (\boldsymbol{x}_i - \boldsymbol{x}_j)/\lvert\boldsymbol{x}_i - \boldsymbol{x}_j\rvert$, $\boldsymbol{v}_{rel} = \boldsymbol{v}_i - \boldsymbol{v}_j + \boldsymbol{\omega}_i \times \boldsymbol{R}_i - \boldsymbol{\omega}_j \times \boldsymbol{R}_j$, $\boldsymbol{\omega}_{rel} = \boldsymbol{\omega}_i - \boldsymbol{\omega}_j$, $\boldsymbol{v}_{n,rel} = (\boldsymbol{v}_{rel}\cdot\hat{\boldsymbol{n}}_{ij})\hat{\boldsymbol{n}}_{ij}$, $\boldsymbol{v}_{t,rel} = (\boldsymbol{v}_{rel}\times\hat{\boldsymbol{n}}_{ij})\times\hat{\boldsymbol{n}}_{ij}$, $\hat{\boldsymbol{t}}_{ij} = \boldsymbol{v}_{t,rel}/\lvert\boldsymbol{v}_{t,rel}\rvert$, $\boldsymbol{R}_i = -R_i\hat{\boldsymbol{n}}_{ij}$ The integration of tangential overlap $\int\delta_t\hat{\boldsymbol{t}}_{ij}$ is truncated to fulfill $\lvert\boldsymbol{F}^c_{t,ij}\rvert \le \mu\lvert\boldsymbol{F}^c_{n,ij}\rvert$.

Table 2
Models for calculating conductive and radiative heat transfers.

Primary equations	
Conduction flux:	$Q_{ij}^{cond} = Q_{ij}^{pp} + Q_{ij}^{pfp}$
Conduction through contact surface:	$Q_{ij}^{pp} = \frac{4cr_c(T_j-T_i)}{1/k_{p,i}+1/k_{p,j}}$
Conduction through interstitial fluid:	$Q_{ij}^{pfp} = (T_j - T_i)\int_{r_{sij}}^{r_{sf}} \frac{2\pi r dr}{l_s\cdot(1/k_{pi}+1/k_{pj})+l_g/k_f}$
Radiation flux Q_{ij}^{rad}:	$\frac{\sigma(T_j^4-T_i^4)}{(1-\epsilon_{r,i})/(\epsilon_{r,i}A_i)+(1-\epsilon_{r,j})/(\epsilon_{r,j}A_j)+2/(A_i(1+F_{ij}))}$
Secondary equations	
$c = (E^*/E_o^*)^{1/5}$	$l_g = 2[(R+H) - \sqrt{(R^2-r^2)}]$
$H = (d_{ij} - 2R)/2$	$l_s = \sqrt{R^2-r^2} - r(R+H)/r_{ij}$
$r_{ij} = 0.560R(1-\epsilon)^{-\frac{1}{3}}$	$r_{sf} = \frac{R\,r_{ij}}{\sqrt{r_{ij}^2+(R+H)^2}}$
$r_{sij} = r_c$ if $H < 0$	$F_{ij} = C_1\left(\frac{d_{ij}}{R}\right)^{C_2} + C_3$ if $H \ge 0$
$r_{sij} = 0$ if $H \ge 0$	$F_{ij} = 0.4\frac{d_{ij}}{R} + 0.215\alpha_s - 0.42$ if $H < 0$
$C_1 = 0.1755 + 6.65\alpha_s$	$C_2 = -0.9373 - 2.899\alpha_s$
$\alpha_s = 1 - \epsilon$	$C_3 = -0.2923 + 0.2487\alpha_s$

of the auger reactor since the major forces arise from mechanical torques by the shaft. The mechanical forces are transferred by particle-particle contact/collision and particle-wall contact/collision in the bed. The equations for calculating forces and torques acting on particle i are summarized in Table 1.

The mass of biomass particles is not a constant and varies in the process of thermochemcial decomposition of the biomass material. Biomass is originally composed of four major components: hemicellulose, cellulose, lignin and moisture. In the pyrolysis process, solid, liquid and gas species are involved and a variety of intermediate species are produced and consumed as illustrated in Fig. 1. The particle mass is composed of all solid species and liquids including biomass original components, intermediate solid species, solid products and liquid water. Gaseous species include products such as water vapor, non-condensable gases and tar vapor. The produced water vapor, non-condensable gas and tar vapor emit for the particle surface immediately and cause the reduction of particle mass. In the pyrolysis of a biomass particle, the thermochemical conversion process progresses gradually into the biomass core from outside. When the particle is small, this process is very fast and negligible. In the current DEM simulation, the mass loss of the biomass particle is considered uniform across the particle. The mass change rate of particle i is formulated as

$$\frac{dm_i}{dt} = \frac{dm^p_{water}}{dt} - \dot{r}_{gas} - \dot{r}_{tar}, \tag{3}$$

where, the first term on the right hand side accounts for the water evaporation from the particle, $\dot{r}_{gas}$ and $\dot{r}_{tar}$ are the production rates for non-condensable gas and tar arising from the biomass pyrolysis.

2.2.2. Interparticle heat transfer

In current approach, the intraparticle transport phenomena are not resolved for particles and the particles are considered as isothermal. The energy equation for particle i is written as

$$m_i c_{p,i}\frac{dT_i}{dt} = \sum_j Q_{ij}^{cond} + \sum_j Q_{ij}^{rad} + Q_{fi}^{conv} - \sum_r \Delta H_r \dot{w}_r, \tag{4}$$

where, $c_{p,i}$ is the mass-weighted specific heat capacity of the solid species, Q_{ij}^{cond} and Q_{ij}^{rad} are conductive and radiative heat transfer between particle i and j, respectively. ΔH_r and $\dot{w}_r$ are the heat of reaction and the reaction rate of reaction r. The fluid movement relative to the particles is ignored in the auger-driven moving bed and, as a result, the convective heat transfer Q_{fi}^{conv} between the fluid and particles i is not included. The heat transfer models for predicting Q_{ij}^{cond} and Q_{ij}^{rad} have already been described in our previous research [11]. The heat transfer models accounting for the heat conduction through interstitial fluid and the heat radiation between two spheres are based on the double taper cone model [37,38]. Therefore, the geometry parameters (seen in Table 2) such as radiating surface area A_i are defined therein. Property parameters such as k_p, E and ϵ_r are specified in Table 3. Parameters ϵ and

α_s are defined as local porosity and solid fraction, separately. The equations for the heat transfer model are organized in Table 2.

It is worth mentioning that the validation of the heat transfer models are already discussed in our previous paper [11]. Interested readers could refer to this paper for more details.

2.2.3. Mass equation of species

Fig. 1 illustrates the thermochemical conversion from biomass components to gaseous and solid products. Since particles are assumed to be isothermal, gaseous products leave the solid particles immediately after production and no intraparticle transport is included.

For solid species, the mass balance is written as

$$\frac{\partial m_{si}^p}{\partial t} = \dot{r}_{si} \quad i = 1, \ldots, n_s, \tag{5}$$

where, m_{si}^p is the mass of solid species i, $\dot{r}_{si}$ is the net production rate of the solid species. For liquid phase, a similar mass balance is written as

$$\frac{\partial m_{li}^p}{\partial t} = \dot{r}_{li} \quad i = 1, \ldots, n_l, \tag{6}$$

where, m_{li} is the mass of liquid species i, $\dot{r}_{li}$ is the net production rate of liquid species i. For vapor species, the accumulated mass leaving a particle is calculated as

$$\frac{\partial m_{vi}}{\partial t} = \dot{r}_{vi} \quad i = 1, \ldots, n_v, \tag{7}$$

and m_{vi} is the accumulated mass of gaseous species i emitted from a particle, $\dot{r}_{vi}$ is the net production rate of gaseous species.

2.3. Pyrolysis kinetics

Adopting mechanistic kinetics could provide detailed reaction information of the biomass conversion process but requires extensive computational time. To balance the reaction detail and computational time, a multiple-component reaction scheme that was proposed by Calonaci et al. [39] is adopted in this research. This reaction kinetics assumes the decomposition processes of the hemicellulose, cellulose and lignin are independent and the pyrolysis of biomass is modeled via a superposition of cellulose, hemicellulose and lignin kinetics. The reaction pathway is illustrated in Fig. 3 and the reaction parameters are available in Table A.1 in the Appendix. The heat of reaction parameter is over-estimated in [39] and the refitted parameter from their another research [40] is used. In this research, we focus on the biomass primary decomposition kinetics, the secondary reactions occurring in the gas phase are not modeled.

All the kinetic reactions are first order. The reaction rate of reaction r is written as

$$\dot{w}_r = A_r \exp\left(-\frac{E_r}{R_g T_p}\right) m_r^p, \tag{8}$$

where, A_r, E_r and R_g are the frequency factor, the activate energy and the gas constant for reaction r, m_r^p is the mass of reactant in the particle. The production rate of each species is written in terms of reaction rate $\dot{w}_r$ accordingly.

2.4. Particle properties

In the biomass pyrolysis process, biomass properties such as particle porosity and thermal conductivity are functions of biomass conversion process and temperature. Biomass conversion degree is formulated as

$$X = 1 - \frac{m_b}{m_{b,0}}, \tag{9}$$

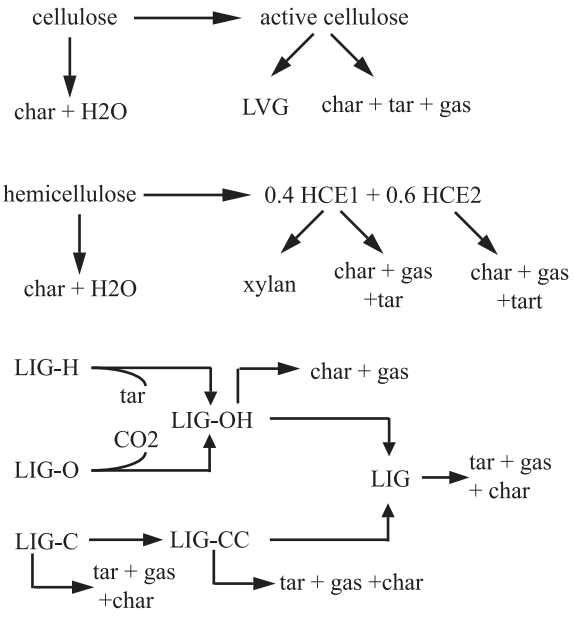

Fig. 3. Illustration of biomass pyrolysis scheme developed in [39].

where, $m_{b,0}$ is the initial biomass mass. The biomass particle thermal conductivity is written as

$$k_{p,b} = (1 - X)k_b + Xk_{char}. \tag{10}$$

In the equation, k_b and k_{char} refer to the biomass and char (solid product) thermal conductivities, respectively. The thermal conductivities for biomass and char remained 0.2 and 0.1 W/(m · K). The specific heat capacities for the biomass components and solid products (char) are [41]:

$$c_{p,b} = 1500 + T_p, \tag{11}$$

$$c_{p,char} = 420 + 2.09T_p + 6.85 \times 10^{-4} T_b^2. \tag{12}$$

Other physical and thermodynamic properties of biomass and sand materials such as Young's modulus, Poisson's ratio, coefficient of restitution and thermal emissivity are listed in Table 3. Properties such as Young's modulus and Poisson's ratio are expected to change with particle structure and composition but both parameters remain constant in current DEM simulations for simplicity.

2.5. Initial and boundary conditions

The inlet mass flow rate of biomass particles is varied from 1 kg/h to 3 kg/h for instigating the effects of volumetric fill level

Table 3
Red oak (biomass), sand, and steel mechanical and thermal properties in DEM.

Material*	Red oak	Sand	Steel
Material mechanical properties			
Initial Density ρ (kg/m^3)	550	2680	-
Young's Modulus E (Pa)	6.0×10^6	6.0×10^6	6.0×10^6
Original Young's Modulus E_o (Pa)	1.2×10^{10}	7.0×10^{10}	2.0×10^{11}
Poisson's ratio ν	0.29	0.25	0.3
Coefficient of restitution e	0.4	0.65	0.65
Coefficient of friction μ	0.2		
Coefficient of rolling friction μ_r	1×10^{-4}		
Material thermal properties			
Conductivity k $\left(\frac{W}{m \cdot K}\right)$[a]	0.2	1.3	38
Specific heat capacity c_p $\left(\frac{W}{kg \cdot K}\right)$	$1500 + T_p$	830	490
Emissivity ϵ_r	0.9	0.8	0.8

[a] The fluid thermal conductivity is 0.039 W/(m · K).

on the biomass fast pyrolysis process. However, the comparisons of predicted product yields with experimental measurements are conducted based on the inlet mass flow rate of 1 kg/h, which remains the same as the biomass feeding rate in experiments [8,34]. Different sizes of biomass particles are adopted in simulations in order to investigate its effects on the fast pryolysis process. Inlet temperatures of biomass and sand particles are set to 300 K and 848 K, separately. Based on energy balance analysis in ideal mixing scenario, the ratio of inlet sand mass flow rate to inlet biomass mass flow rate is determined to be 15:1 in order to achieve an optimal fast pyrolysis reaction temperature, which is reported to be around 788 K [8,34]. The size of sand particles is identical to the size of biomass particles in all simulations. Initially, there is no biomass or sand particle present in the reactor.

The initial composition of the red oak biomass is 42.75 wt% in cellulose, 26.325 wt% in hemicellulose, 20.925 wt% in lignin and 10 wt% in moisture for all simulations. The mass percentage distribution among cellulose, hemicellulose and lignin in red oak is extracted from [42] without inclusion of extractives. The lignin mass percentage is assumed to evenly distributed among three types of lignins: carbon-rich lignin (LIGC), hydrogen-rich lignin (LIGH) and oxygen-rich lignin (LIGO), which gives 62.4 wt% C, 32 wt% O and 5.6 wt% H in lignin. While this treatment generates a satisfactory approximation to the elemental analysis of lignin reported in [43], the inconsistent results of different lignin extraction methods make it very difficult to quantify the real distribution of LIGC, LIGH and LIGO in red oak biomass.

A fixed temperature boundary condition is applied at the reactor trough wall and the auger walls are treated as adiabatic. The reactor trough wall temperature is determined to be the same as the calculated fast pyrolysis reaction temperature, which is determined to be $T_w = 788$ K. The same boundary condition was also adopted for the reactor wall in previous experimental studies [8,34].

2.6. Numerical algorithms

The implementation of the extended DEM is based on the LIGGGHTS software [44]. A fixed time step of 2.5×10^{-6} s for updating particle position and temperature is adopted which could guarantee the time step is less than 20% of critical time step determined from the Rayleigh wave speed of force transmission [45]. The critical time is formulated as

$$\Delta t = \frac{\pi R}{0.8766 + 0.1631\nu}\sqrt{\frac{\rho}{G}}. \tag{13}$$

The Verlet integration method is adopted for integrating particle motion equations. The runge-kutta-dopri5 ordinary differential equation (ODE) solver in the odeint code [46] is incorporated in the algorithm to integrate the reaction ODEs. Considering the large variation of time scales of different reactions, the time step for ODE integration is adaptive as shown in Fig. 4. In general, the reaction ODE integration takes a larger time step (m times larger) than particle motion integration. However, reaction integration time step is automatically reduced when the temperature change due to the heat of reaction source (see Eq. 4) exceeds a set point in one time step. Significant amount of heat sink or source was found to cause instability in the temperature prediction from the energy equation. The proposed adaptive time step method could prevent the stability issue and reduce the computational burden of adopting a smaller fixed time step for all the particles in the whole simulation time.

3. Results and discussion

The biomass fast pyrolysis process is affected by particle properties such as particle size and moisture content, and operating

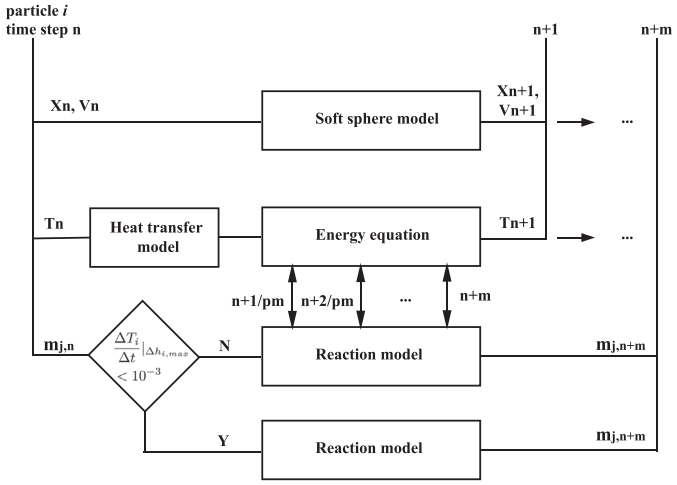

Fig. 4. Implemented algorithm of adaptive time step size for the reaction model. The reaction model takes $m\Delta t$ time step size at the beginning of each integration, where Δt is the DEM time step size. If the integration condition $\Delta T_i/\Delta t_r|_{\Delta h_i} < 10^{-3}$ is not met, the integration time step size Δt_r for the reaction model is decreased by half and the time step reduction continues recursively until the integration condition is met. p is the resultant number of steps for reaction integration within $m\Delta t$ time.

conditions such as heating rate and volumetric fill level in the reactor. However, the current research is not intended for a thorough parameter study. Instead, the applicability of the approach to simulating biomass fast pyrolysis is examined in this section, which covers the validation of the kinetic model, the comparison of numerical predictions of biomass thermal decomposition kinetics with experimental measurements, and the scalability performance of the approach in modeling different system sizes. The rotational speed of the augers in current research is fixed at 40 RPM and the mass feeding ratio of biomass to sand materials remains 1:15. Simulation results reveal that the reactor reaches steady state in 30 s, after which the results presented in the following were extracted. The influences of two parameters, particle size and volumetric fill level, are evaluated on the biomass fast pyrolysis process, which provides useful insights on the heat and mass transport process in the reactor.

3.1. Validation of Ranzi's kinetic model implementation

As mentioned, Ranzi's kinetics is adopted to predict biomass thermal decomposition dynamics. The implementation of the kinetic model is first validated by comparing predictions of cellulose, hemicellulose, hardwood and softwood pyrolysis process with experimental results, as similarly carried out in [47]. The simulations were conducted on a static single biomass particle, which is heated up at prescribed heating rates as specified in Fig. 5. The model accuracy is assessed by a mean deviation parameter that is defined as [24]

$$MD = \frac{1}{n}\sum_{i=1}^{n}|X_{exp,i} - X_{model,i}|, \tag{14}$$

where n is the number of data points and $X_{model,i}$ and $X_{exp,i}$ are the same variable predicted by the DEM model and measured in experiments, separately.

In the simulation, the hardwood composition is accounted for by 49.8 wt% cellulose, 33.2 wt% hemicellulose and 17.0 wt% lignin while the composition of the softwood is 40.1 wt% cellulose, 26.7 wt% hemicellulose and 33.2 wt% lignin, according to [47]. Fig. 5 shows comparisons of the solid residue profiles measured in experiments [48–50] and predicted by the model in the pyrolysis

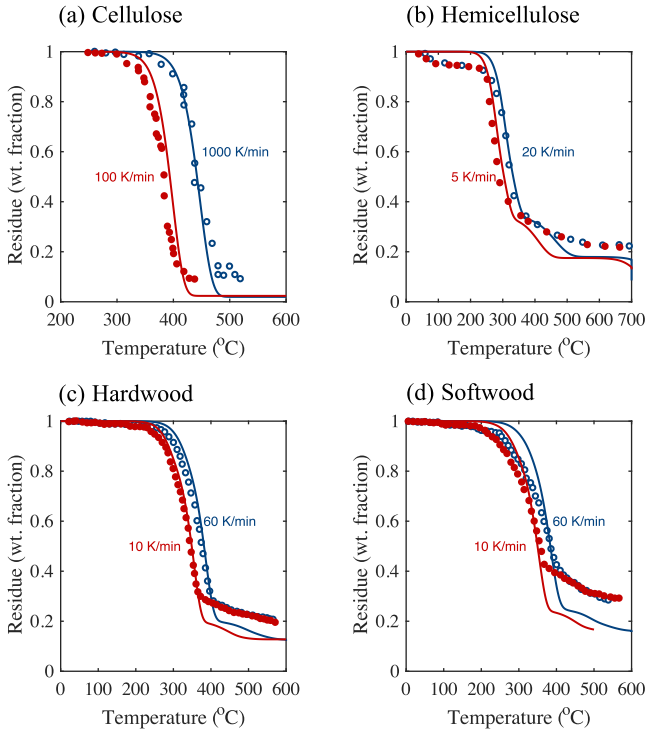

Fig. 5. Comparisons of Ranzi's kinetic model predictions and experimental data. (a) pyrolysis of cellulose; (b) pyrolysis of hemicellulose; (c) pyrolysis of hardwood; (d) pyrolysis of softwood. Lines in all figures are from numerical predictions and points are experimental data from [48] in (a), [49] in (b), and [50] in (c) and (d), separately.

of cellulose, hemicellulose, hardwood and softwood biomass. The variations of the solid residue with the temperature are satisfactorily predicted based on visual check, especially for the hardwood biomass. Some discrepancies are observed at high temperatures, which mostly inherits from the original kinetic model as seen in the comparison study [47] and some other differences might come from the slight modification of the kinetics [39]The calculated MDs for cellulose predictions are 0.081 for 100 K/min heating rate and 0.056 for 1000 K/min heating rate. The MDs of hemicellulose predictions are 0.057 for 5 K/min heating rate and 0.04 for 20 K/min heating rate. The MDs of hardwood predictions are 0.0405 and 0.0364 at the heat rates of 10 K/min and 60 K/min separately, while the MDs are 0.07 and 0.061 for softwood predictions at the same heating rates as for the hardwood. The quantitative assessment of the Ranzi's kinetic model suggests that this kinetic model gives satisfactory performance in the prediction of hardwood pyrolysis.

3.2. Biomass temperature and mass loss profiles

Fig. 6 shows the biomass temperature and mass loss profiles along the axial direction of the reactor from two simulations with different particle sizes. The biomass residue mass is composed of fresh biomass components (cellulose, hemicellulose and lignins) and intermediate species of each component (CELLA, HCE1, HCE2, LIGCC, LIG and LIG-OH in Table A.2), and is scaled by the original biomass mass m_0 in the Figure. As expected, the biomass temperature is gradually heated up as the biomass is transported in the axial direction by the augers in both cases. However, the degree of the pyrolysis process is noticeably different. In the simulated system with particle size of 2 mm, 8.6 wt% of intermediate species is not converted into final products at the end of the reactor. Comparison of the profiles in Fig. 6 (a) and (b) indicates that decreasing particle size could improve both biomass heating rate and fast pyrolysis process.

The volumetric fill level in the auger reactor has noticeable influences on the particle mixing and heat transfer process as discussed in our previous paper [10,11]. The volumetric fill level is calculated from the total volume of particles and the void space in a representative reactor element, which is defined as

$$f = \frac{\pi d_p^3 N/6}{0.56V}, \tag{15}$$

where, N is the averaged particle number and V is the volume of the void space in a reactor element. Since the reactor geometry repeats itself in an auger pitch length in the axial direction, the representative reactor element is chosen to be an auger pitch length segment in the middle of the reactor. The packing density of particles is characterized by the solid fraction parameter, which is estimated to be close to very loose random packing value of 0.56.

The effect of the volumetric fill level on the pyrolysis process is evaluated and predicted results are compared in Fig. 7, in which the biomass temperature and mass loss profiles at two different volumetric fill levels are shown. The result indicates that the biomass temperature slope decreases at increased volumetric fill level and, as a result, the biomass fast pyrolysis process is slowed down. Our previous research observes that the heat transfer coefficient (h) remains constant when $x/D > 6$ under the same operating conditions [11]. It is interesting to notice that the biomass mass loss curve is very close to a constant when $x/D > 6$ in both Fig. 7 (a) and (b). The observation suggests that the biomass decomposition process is linearly related with the heat transfer coefficient and the biomass fast pyrolysis process at particle size $d_p = 2$ mm is dominated by the heat transport process.

To quantitatively evaluate the limiting factor in the biomass fast pyrolysis process, a Py number is defined as

$$\mathrm{Py} = \frac{\tau_{\mathrm{reaction}}}{\tau_{\mathrm{heat}}} = \frac{h}{\rho C_p l_c k_r}, \tag{16}$$

where, τ_{reaction} refers to the reaction time scale and τ_{heat} is the heat transfer time scale; h is the heat transfer coefficient for biomass particles; l_c is the characteristic length of the particle and is equal to the particle diameter d_p; k_r is the mass loss rate of biomass defined as $d(m/m_o)/dt$ with m_o being the biomass original mass. With extracted heat transfer coefficient $h = 103$ W/(m$^2 \cdot$ K) and mass loss rate $k_r = 0.1875$ s^{-1} from the simulation, the Py number is estimated to be around 0.22 at the operating condition in Fig. 7 (a). The Py number indicates that the time scale for the heat transfer is much longer than the reaction time scale and the biomass fast pyrolysis process in the reactor is heat transport dominated process at particle size $d_p = 2$ mm.

3.3. Thermochemical decomposition dynamics of biomass components

Fig. 8 shows the averaged mass loss rate of biomass major components: moisture, hemicellulose, cellulose and lignin. The hemicellulose mass is composed of origin hemicellulose and activated hemicellulose, the cellulose mass is the summation of origin cellulose and activated cellulose, and the lignin mass is composed of three original lignin forms (oxygen-rich lignin LIG-O, hydrogen-rich lignin LIG-H, carbon-rich lignin LIGC), carbon-rich lignin (LIGCC), OH-rich lignin (LIGOH) and lignin (LIG).

It is observed that the moisture starts to evaporate at the biomass feed inlet position ($x/D = 2.0$) and shows a peak before the sand feed inlet position ($x/D = 4.0$) when pyrolyzing biomass particles with size of 1 mm. For biomass particles with size of 2 mm, the moisture evaporation reaches the peak around $x/D = 4.0$ at both high and low volumetric fill levels. However, the duration of moisture evaporation at higher volumetric fill level ($f =$

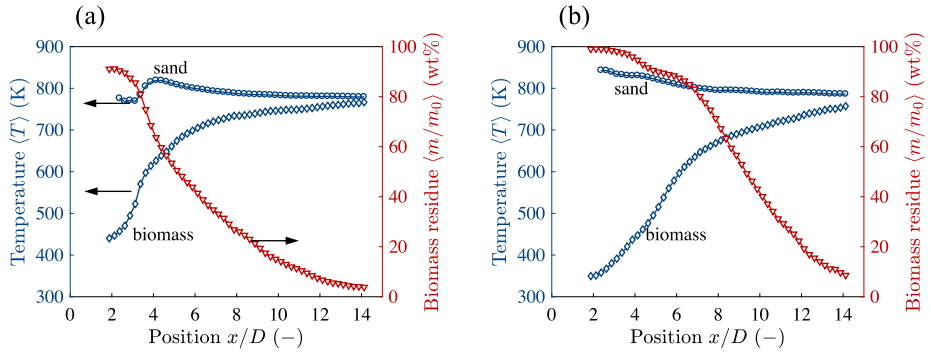

Fig. 6. Predictions of biomass pyrolysis process with particle size: (a) $d_p = 1$ mm and (b) $d_p = 2$ mm. Operating condition: volumetric fill level $f = 0.1$ and moisture content 10%.

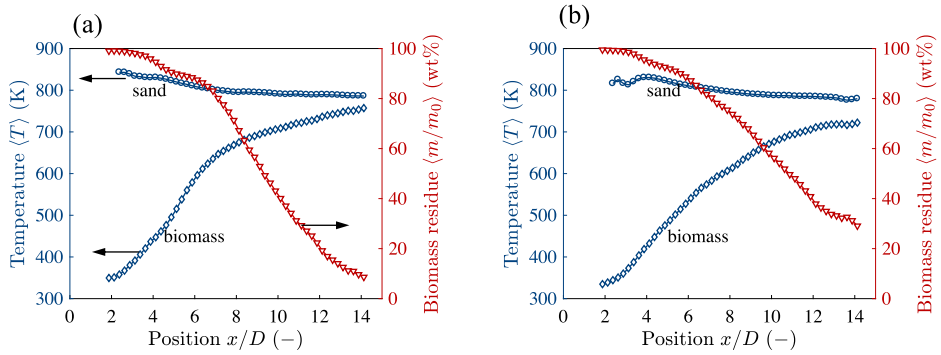

Fig. 7. Predictions of biomass pyrolysis process at volumetric fill level (a) $f = 0.1$ and (b) $f = 0.37$. Operating condition: particle size $d_p = 2$ mm, moisture content 10%.

0.37) increases. While the moisture evaporation is well separated from biomass thermochemical decomposition in Fig. 8 (b), the two processes have overlaps in both Fig. 8 (a) and (c). A smaller particle size is adopted in Fig. 8 (a) and a faster heating rate is observed, which causes the overlap of moisture evaporation and biomass solid species decomposition. The non-ideal particle mixing and particle mixing oscillation (seen in [10]) at higher volumetric fill level result in nonhomogeneous heating process of biomass particles. As a result, the overlap of the moisture evaporation and biomass solid species decomposition is observed in Fig. 8 (c). Both hemicellulose and lignin decomposition start around 480 K and cellulose starts to decompose around 600 K as read in Fig. 8 (b). This prediction is consistent with experimental observations in [51]. The mass loss peak for hemicellulose and cellulose occurs around 600 K for particle size of 1 mm while the peak is around 650 K for particle size of 2 mm as shown in Fig. 8 (a) and (b). The initial decomposition temperature for cellulose seems to be lower in Fig. 8 (c), which is apparently caused by the nonhomogeneous heating process at higher fill level. A fraction of biomass particles reach the cellulose decomposition temperature while the average temperature is still below that temperature as a result of nonhomogeneous heating process. The decomposition of all three components has a wide temperature range due to heat transfer and reaction time limitations. The result also indicates a higher mass loss rate with a smaller particle size by comparing Fig. 8 (a) and (b), and decreasing volumetric fill level is favorable to the biomass pyrolysis.

3.4. Product yield

Two simulations of red oak fast pyrolysis in the double auger reactor were conducted at the biomass feeding rate of 1 kg/h with particle size of 1 mm (Fine particle) and 2 mm (Coarse particle), separately. Other initial and boundary conditions are specified in Section 2.5. As the biomass is gradually pyrolyzed along the axial direction, vapor products are released from solid biomass and finally condensed into products of bio-oil and noncondensable gas (NC gas) at room temperature. In the process, char is also produced and remains in the solid state. The major components of each product are listed in Table A.2 in the Appendix. Fig. 9 shows the accumulated mass percentage profiles of tar vapor (condensed into bio-oil) and noncondensable gas releasing from biomass particles, and char mass percentage profiles along the axial direction. In the figure, the water vapor is excluded from tar vapor in order to show the moisture evaporation process and the char product includes all the solid species except the original biomass components. The results confirm that reducing biomass particle size is favorable for speeding up the biomass decomposition process in the auger reactor.

In order to compare with experimental results, the predicted yields of bio-oil (with reaction water), char and NC gas are calculated as mass percentage of dry biomass and are shown in Fig. 10. The model predictions are compared with the experimental data reported in [8], in which two sand particle sizes were used with fine sand in the size range of 250–600 μm and coarse sand in the size range of 600–1000 μm. It is observed that the predicted product yields are very close to the experimental results, especially in the comparison with fine particle simulation results. The mean deviations are 2.49 wt%, 1.68 wt% and 1.42 wt% for the bio-oil, char and NC gas yield predictions, separately. The yield predictions are in reasonable agreement with experimental results considering the limitations of the biomass pyrolysis kinetics available in the literature. It is worth knowing that no error bar is added to the simulation result since trivial deviations are obtained in the statistical analysis of simulation results.

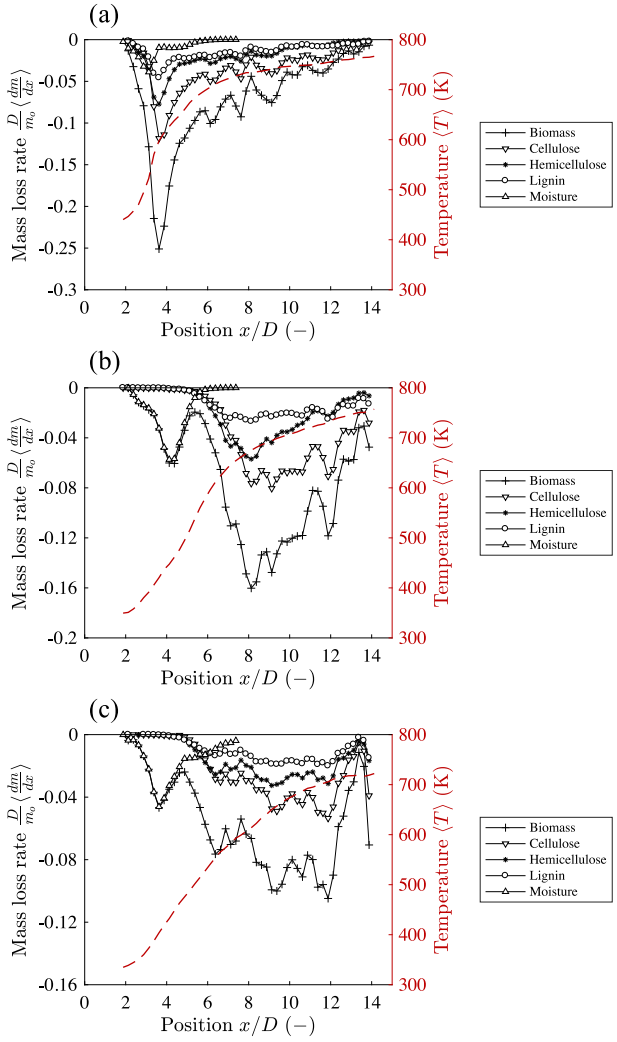

Fig. 8. Non-dimensional mass loss rate of biomass major components. Operating condition: (a) particle size $d_p = 1$ mm, volumetric fill level $f = 0.1$; (b) $d_p = 2$ mm, $f = 0.1$; (c) $d_p = 2$ mm, $f = 0.37$. Moisture content is 10% in (a), (b) and (c).

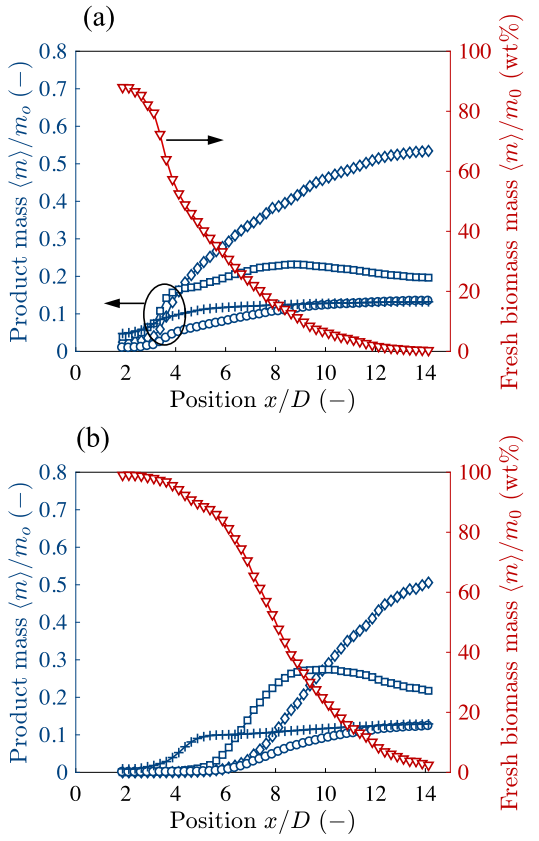

Fig. 9. Prediction of product mass percentage in terms of biomass original mass with particle size of (a) $d_p = 1$ mm and (b) $d_p = 2$ mm, separately. Symbols in the figure: ▽: biomass, ◇: tar vapor (without water vapor), + : water vapor, □: char, and ○: non-condensable gas. Other operating conditions: volumetric fill level $f = 0.1$, biomass moisture content 10%.

3.5. Scalability performance

The scalability test was carried out by fixing the same operating conditions while changing the system size (the amount of particles). At low volumetric fill level $f = 0.1$, the influences of particle mixing on the heat transfer and biomass pyrolysis are very limited, which is suitable to serve as the base operating condition in the test. Three different systems containing approximately 5000, 52500 and 531,000 amounts of particles are generated by varying the particle size parameter but maintaining the same volumetric fill level. The integration time interval of reaction ODEs is set to 50 times of DEM time step interval in all test cases. The simulations were conducted using 16 cores on a cluster node containing two 2.0 GHz 8-core Intel E5 2650 CPU. Moreover, the simulations were all run with the same uniform partition in x and y directions. Fig. 11 presents the elapsed CPU time per 10,000 simulation steps in terms of system size after the system reaches steady state in the simulation. A linear augmentation of computational cost is suggested when the system size increases. The result is helpful to estimating the required CPU times in the simulation of different size systems. To make a comparison with previous research [28], the CPU time required to simulate a system of 800,000 particles for 5 s is estimated to be around 10,000 CPU hours with our developed approach, while a 32 times higher CPU time was reported in [28] for 5 s simulation of a fluidized particulate system. Although the simulated systems are different and a direct comparison is not carried out, the comparison result still reflects the merit of the adaptive time step algorithm, considering that the heavy compu-

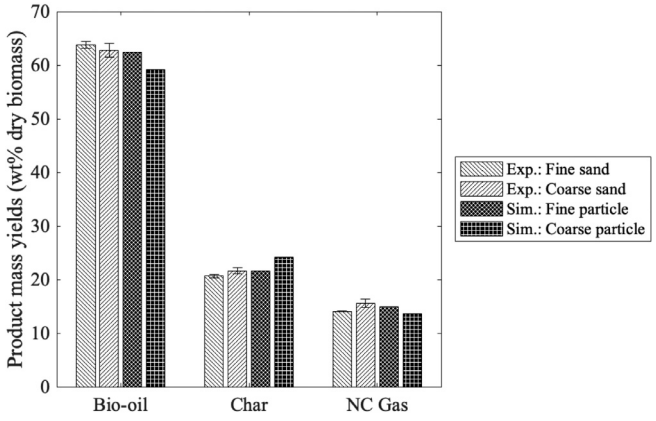

Fig. 10. Predicted product yields from DEM simulations and comparisons with experimental results [8]. The yields are calculated based on dry biomass and the bio-oil contains water generated from reactions.

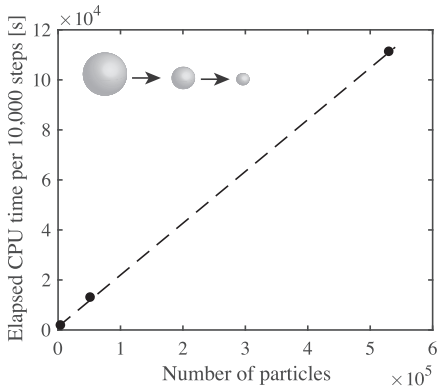

Fig. 11. Scalability performance of the extended DEM approach. Different system sizes are achieved by varying particle size and remaining the same operation condition: volumetric fill level $f = 0.1$, biomass moisture content 10%.

tational cost is usually on the DEM side in a computational fluid dynamics (CFD) and DEM coupling approach.

4. Conclusion

In this research, an extended DEM model is proposed for simulating biomass fast pyrolysis reacting granular flows in a double auger reactor, in which particle hydrodynamics and interparticle heat transfer processes are involved and coupled with chemical reactions in solid particles. An adaptive time step algorithm is proposed to achieve a stable coupling between the integration of reaction ODEs and the DEM solver, and the algorithm is proven computationally efficient.

The proposed method was applied to simulating biomass fast pyrolysis process in a double auger reactor. The implementation of the kinetic model is first validated by carrying out benchmark simulations of a single biomass particle heated at prescribed heating rates and comparing predicted mass loss profiles with experimental data. The comparison indicates that the Ranzi's kinetic model has a satisfactory performance in modeling hardwood pyrolysis process. Moreover, the product yields predicted from simulating the red oak fast pyrolysis in the reactor are in reasonable agreement with the experimental results, which evidences that the extended DEM approach is capable of modeling biomass pyrolysis process in the double auger reactor. The analysis of the pyrolysis number Py suggests that the limiting factor in the biomass fast pyrolysis arises from external heat transfer to the biomass particles. The hemicellulose and cellulose decomposition temperatures are predicted to be around 480 K and 600 K separately and the predictions are in agreement with experimental studies.

The biomass fast pyrolysis process in the auger reactor is significantly influenced by the heat of reaction parameter in the kinetic model. In future work, careful calibration of the heat of reaction parameter is necessary for improvement of biomass fast pyrolysis kinetic models. The approach reported in [52–54] can be adopted to carry out parameter estimate of the heat of reaction.

In current study, the biomass particle is assumed to have a spherical shape and the predicted product yields are in agreement with experimental results. In reality, the biomass particles usually have nonsymmetric shapes. Modeling the complexity in the hydrodynamics of nonspherical particles and the interparticle heat transfer process is overwhelming but necessary in future research.

Conflict of interest

The authors declare no conflicts of interest to this work.

CRediT authorship contribution statement

Fenglei Qi: Conceptualization, Methodology, Software, Validation, Formal analysis, Investigation, Data curation, Writing - original draft, Visualization. **Mark Mba Wright:** Resources, Writing - review & editing, Supervision, Project administration, Funding acquisition.

Acknowledgements

The research reported in this paper is partially supported by the HPC@ISU equipment at Iowa State University, some of which has been purchased through funding provided by NSF under MRI grant number CNS 1229081 and CRI grant number 1205413.

Funding: This work was supported by the National Science Foundation EPSCoR program [grant EPS-1101284].

Appendix

Table A1
Biomass pyrolysis kinetics.

	Reaction	A (s^{-1})	E (kJ mol^{-1})	Δh (kJ kg^{-1})
1	CELL → CELLA	8×10^{13}	192.5	0
2	CELL → 5 H_2O + 6 Char	8×10^{7}	133.9	-1913
3	CELLA → 0.95 HAA + 0.25 GLYOX + 0.2 CH_3CHO + 0.25 HMFU +0.2 C_3H_6O + 0.16 CO_2 + 0.23 CO + 0.9 H_2O + 0.1 CH_4 + 0.61 Char	1×10^{9}	125.5	620
4	CELLA → LVG	4*T*	41.8	364
5	HCE → 0.4 HCE1 + 0.6 HCE2	1×10^{10}	129.7	100
6	HCE1 → 0.75 G{H_2} + 0.8 CO_2 + 1.4 CO + 0.5 CH_2O + 0.25 CH_3OH +0.125 ETOH + 0.125 H_2O + 0.625 CH_4 + 0.25 C_2H_4 + 0.675 Char	3×10^{9}	113.0	-92
7	HCE1 → XYL	3*T*	46.0	588
8	HCE2 → 0.2 CO_2 + 0.5 CH_4 + 0.25 C_2H_4 + 0.8 G{CO_2} + 0.8 G{COH_2} +0.7 CH_2O + 0.25 CH_3OH + 0.125 ETOH + 0.125 H_2O + Char	1×10^{10}	138.1	212
9	LIGC → 0.35 LIGCC + 0.1 pCOUMARYL + 0.08 PHENOL + 0.41 C_2H_4 +H_2O + 0.495 CH_4 + 0.32 CO + G{COH_2} + 5.735 Char	4×10^{15}	202.9	-490
10	LIGH → LIGOH + C_3H_6O	2×10^{13}	156.9	100
11	LIGO → LIGOH + CO_2	1×10^{9}	106.7	446
12	LIGCC → 0.3 pCOUMARYL + 0.2 PHENOL + 0.35 $C_3H_4O_2$ + 0.7 H_2O +0.65 CH_4 + 0.6 C_2H_4 + G{COH_2} + 0.8 G{CO} + 6.4 Char	5×10^{6}	131.8	-503
13	LIGOH → LIG + H_2O + CH_3OH + 0.45 CH_4 + 0.2 C_2H_4 + 1.4 G{CO} +0.6 G{COH_2} + 0.1 G{H_2} + 4.15 Char	3×10^{8}	125.5	-120
14	LIG → FE2MACR	8*T*	50.2	686
15	LIG → H_2O + 0.5 CO + 0.2 CH_2O + 0.4 CH_3OH + 0.2 CH_3CHO +0.2 C_3H_6O + 0.6 CH_4 + 0.65 C_2H_4 + G{CO} + 0.5 G{COH_2} + 5.5 Char	1.2×10^{9}	125.5	-470
16	G{CO_2} → CO_2	1×10^{5}	100.4	0.0
17	G{CO} → CO	1×10^{13}	209.2	0.0
18	G{COH_2} → CO + H_2	5×10^{11}	272.0	0.0
19	G{H_2} → H_2	5×10^{11}	313.8	0.0
20	$H_2O(l)$ → $H_2O(g)$	5.43×10^{10}	880	2440

Table A2
Solid, liquid and gaseous species in Ranzi's pyrolysis model.

Species	Name	Atomic composition
Solid species		
Solid biomass components:		
CELL	Cellulose	$C_6H_{10}O_5$
HCE	Hemicellulose	$C_5H_8O_4$
LIGC	Carbon-rich lignin	$C_{15}H_{14}O_4$
LIGH	Hydrogen-rich lignin	$C_{22}H_{28}O_9$
LIGO	Oxygen-rich lignin	$C_{20}H_{22}O_{10}$
Solid products:		
CELLA	Activated cellulose	$C_6H_{10}O_5$
HCE1	Activated hemicellulose 1	$C_5H_8O_4$
HCE2	Activated hemicellulose 2	$C_5H_8O_4$
LIGCC	Carbin-rich lignin 2	$C_{15}H_{14}O_4$
LIG	Lignin	$C_{11}H_{12}O_8$
LIGOH	OH-rich lignin	$C_{19}H_{22}O_8$
G{CO_2}	Trapped CO_2	CO_2
G{CO}	Trapped CO	CO
G{COH_2}	Trapped COH_2	COH_2
G{H_2}	Trapped H_2	H_2
Char	Char	C
Liquid species		
H_2O(l)	Moisture	H_2O(l)
Gaseous species		
Condensable vapors (liquid products):		
HAA	Hydroxyacetaldehyde	$C_2H_4O_2$
CLYOX	Glyoxal	$C_2H_2O_2$
C_3H_6O	Propanal (acetone)	C_3H_6O
$C_3H_4O_2$	Propanedial	$C_3H_4O_2$
HMFU	5-Hydroxymethylfurfural	$C_6H_6O_3$
LVG	Levoglucosan	$C_6H_{10}O_5$
XYL	Xylose monomer	$C_5H_8O_4$
pCOUMARYL	Paracoumaryl alcohol	$C_9H_{10}O_2$
PHENOL	Phenol	C_6H_6O
FE2MACR	Sinapaldehyde	$C_{11}H_{12}O_4$
CH_2O	Formaldehyde	CH_2O
CH_3OH	Methanol	CH_4O
CH_3CHO	Acetaldehyde	C_2H_4O
ETOH	Ethanol	C_2H_6O
H_2O	Water vapor	H_2O
Noncondensable vapors (gas products):		
H_2	Hydrogen	H_2
CO	Carbon monoxide	CO
CO_2	Carbon dioxide	CO_2
CH_4	Methane	CH_4
C_2H_4	Ethylene	C_2H_4

(*continued on next page*)

Table A2 (*continued*)

References

[1] C. Stevens, R.C. Brown, Thermochemical processing of biomass: Conversion into Fuels, Chemicals and Power, John Wiley & Sons, 2011.

[2] H. Goyal, D. Seal, R. Saxena, Bio-fuels from thermochemical conversion of renewable resources: a review, Renew. Sustain. Energy Rev. 12 (2) (2008) 504–517.

[3] R. Venderbosch, W. Prins, Fast pyrolysis technology development, Biofuels Bioprod. Biorefining 4 (2) (2010) 178–208.

[4] A. Imran, E. Bramer, K. Seshan, G. Brem, et al., An overview of catalysts in biomass pyrolysis for production of biofuels., Biofuel Res. J. 5 (4) (2018) 872–885.

[5] H.K.S. Panahi, M. Tabatabaei, M. Aghbashlo, M. Dehhaghi, M. Rehan, A.-S. Nizami, Recent updates on the production and upgrading of bio-crude oil from microalgae, Bioresource Technol. Rep. 7 (2019) 100216.

[6] E. Butler, G. Devlin, D. Meier, K. McDonnell, A review of recent laboratory research and commercial developments in fast pyrolysis and upgrading, Renew. Sustain. Energy Rev. 15 (8) (2011) 4171–4186.

[7] A.V. Bridgwater, Review of fast pyrolysis of biomass and product upgrading, Biomass Bioenergy 38 (2012) 68–94.

[8] T.J. Daugaard, D.L. Dalluge, R.C. Brown, M.M. Wright, Effect of thermophysical properties of heat carriers on performance of a laboratory-scale auger pyrolyzer, Fuel Process. Technol. 176 (2018) 182–189.

[9] S.-S. Liaw, Z. Wang, P. Ndegwa, C. Frear, S. Ha, C.-Z. Li, M. Garcia-Perez, Effect of pyrolysis temperature on the yield and properties of bio-oils obtained from the auger pyrolysis of Douglas Fir wood, J. Analyt. Appl. Pyrolysis 93 (2012) 52–62.

[10] F. Qi, T.J. Heindel, M.M. Wright, Numerical study of particle mixing in a lab-scale screw mixer using the discrete element method, Powder Technol. 308 (2017) 334–345.

[11] F. Qi, M.M. Wright, Particle scale modeling of heat transfer in granular flows in a double screw reactor, Powder Technol. 335 (2018) 18–34.

[12] W. Zhong, A. Yu, G. Zhou, J. Xie, H. Zhang, CFD simulation of dense particulate reaction system: Approaches, recent advances and applications, Chem. Eng. Sci. 140 (2016) 16–43.
[13] C. Wu, B. Yan, Y. Jin, Y. Cheng, Modeling and simulation of chemically reacting flows in gas–solid catalytic and non-catalytic processes, Particuology 8 (6) (2010) 525–530.
[14] Q. Xiong, Y. Yang, F. Xu, Y. Pan, J. Zhang, K. Hong, G. Lorenzini, S. Wang, Overview of computational fluid dynamics simulation of reactor-scale biomass pyrolysis, ACS Sustain. Chem. Eng. 5 (4) (2017) 2783–2798.
[15] D. Lathouwers, J. Bellan, Modeling of dense gas–solid reactive mixtures applied to biomass pyrolysis in a fluidized bed, Int. J. Multiph. Flow 27 (12) (2001) 2155–2187.
[16] S. Gerber, F. Behrendt, M. Oevermann, An Eulerian modeling approach of wood gasification in a bubbling fluidized bed reactor using char as bed material, Fuel 89 (10) (2010) 2903–2917.
[17] Q. Xue, T. Heindel, R. Fox, A CFD model for biomass fast pyrolysis in fluidized-bed reactors, Chem. Eng. Sci. 66 (11) (2011) 2440–2452.
[18] A. Sharma, S. Wang, V. Pareek, H. Yang, D. Zhang, Multi-fluid reactive modeling of fluidized bed pyrolysis process, Chem. Eng. Sci. 123 (2015) 311–321.
[19] Q. Xiong, F. Xu, E. Ramirez, S. Pannala, C.S. Daw, Modeling the impact of bubbling bed hydrodynamics on tar yield and its fluctuations during biomass fast pyrolysis, Fuel 164 (2016) 11–17.
[20] Q. Xiong, J. Zhang, F. Xu, G. Wiggins, C.S. Daw, Coupling daem and cfd for simulating biomass fast pyrolysis in fluidized beds, J. Analyt. Appl. Pyrolysis 117 (2016) 176–181.
[21] H. Zhong, Q. Xiong, Y. Zhu, S. Liang, J. Zhang, B. Niu, X. Zhang, CFD modeling of the effects of particle shrinkage and intra-particle heat conduction on biomass fast pyrolysis, Renew. Energy 141 (2019) 236–245.
[22] Q. Xue, D. Dalluge, T. Heindel, R. Fox, R. Brown, Experimental validation and CFD modeling study of biomass fast pyrolysis in fluidized-bed reactors, Fuel 97 (2012) 757–769.
[23] S. Aramideh, Q. Xiong, S.-C. Kong, R.C. Brown, Numerical simulation of biomass fast pyrolysis in an auger reactor, Fuel 156 (2015) 234–242.
[24] X. Shi, F. Ronsse, R. Nachenius, J.G. Pieters, 3D Eulerian-Eulerian modeling of a screw reactor for biomass thermochemical conversion. part 2: slow pyrolysis for char production, Renew. Energy 143 (2019) 1477–1487.
[25] H. Zhou, G. Flamant, D. Gauthier, DEM-LES simulation of coal combustion in a bubbling fluidized bed part II: coal combustion at the particle level, Chem. Eng. Sci. 59 (20) (2004) 4205–4215.
[26] M. Oevermann, S. Gerber, F. Behrendt, Euler–Lagrange/DEM simulation of wood gasification in a bubbling fluidized bed reactor, Particuology 7 (4) (2009) 307–316.
[27] S. Gerber, M. Oevermann, A two dimensional Euler – Lagrangian model of wood gasification in a charcoal bed–part I: model description and base scenario, Fuel 115 (2014) 385–400.
[28] J. Bruchmüller, B. van Wachem, S. Gu, K. Luo, R. Brown, Modeling the thermochemical degradation of biomass inside a fast pyrolysis fluidized bed reactor, AIChE J. 58 (10) (2012) 3030–3042.
[29] J. Xie, W. Zhong, B. Jin, Y. Shao, Y. Huang, Eulerian-Lagrangian method for three-dimensional simulation of fluidized bed coal gasification, Advanced Powder Technol. 24 (1) (2013) 382–392.
[30] X. Ku, T. Li, T. Løvås, CFD-DEM simulation of biomass gasification with steam in a fluidized bed reactor, Chem. Eng. Sci. 122 (2015) 270–283.
[31] H. Boujjat, S. Rodat, S. Chuayboon, S. Abanades, Numerical simulation of reactive gas-particle flow in a solar jet spouted bed reactor for continuous biomass gasification, Int. J. Heat Mass Transf. 144 (2019) 118572.
[32] S. Yang, H. Wang, Y. Wei, J. Hu, J.W. Chew, Eulerian-Lagrangian simulation of air-steam biomass gasification in a three-dimensional bubbling fluidized gasifier, Energy 181 (2019) 1075–1093.
[33] J. Xie, W. Zhong, Y. Shao, K. Li, Coupling of CFD-DEM and reaction model for 3D fluidized beds, Powder Technol. 353 (2019) 72–83.
[34] J. Brown, R. Brown, Process optimization of an auger pyrolyzer with heat carrier using response surface methodology, Bioresource Technol. 103 (1) (2012) 405–414.
[35] T.A. Kingston, T.J. Heindel, Granular mixing optimization and the influence of operating conditions in a double screw mixer, Powder Technol. 266 (2014) 144–155.
[36] H. Zhu, Z. Zhou, R. Yang, A. Yu, Discrete particle simulation of particulate systems: theoretical developments, Chem. Eng. Sci. 62 (13) (2007) 3378–3396.
[37] G. Cheng, A. Yu, P. Zulli, Evaluation of effective thermal conductivity from the structure of a packed bed, Chem. Eng. Sci. 54 (19) (1999) 4199–4209.
[38] G. Cheng, A. Yu, Particle scale evaluation of the effective thermal conductivity from the structure of a packed bed: radiation heat transfer, Ind. Eng. Chem. Res. 52 (34) (2013) 12202–12211.
[39] M. Calonaci, R. Grana, E. Barker Hemings, G. Bozzano, M. Dente, E. Ranzi, Comprehensive kinetic modeling study of bio-oil formation from fast pyrolysis of biomass, Energy Fuels 24 (10) (2010) 5727–5734.
[40] E. Ranzi, M. Corbetta, F. Manenti, S. Pierucci, Kinetic modeling of the thermal degradation and combustion of biomass, Chem. Eng. Sci. 110 (2014) 2–12.
[41] Y. Haseli, J. Van Oijen, L. De Goey, Modeling biomass particle pyrolysis with temperature-dependent heat of reactions, J. Analyt. Appl. Pyrolysis 90 (2) (2011) 140–154.
[42] J. Konnerth, M. Eiser, A. Jäger, T.K. Bader, K. Hofstetter, J. Follrich, T. Ters, C. Hansmann, R. Wimmer, Macro-and micro-mechanical properties of red oak wood (Quercus rubra L.) treated with hemicellulases, Holzforschung 64 (4) (2010) 447–453.
[43] S. Zhou, Y. Xue, A. Sharma, X. Bai, Lignin valorization through thermochemical conversion: comparison of hardwood, softwood and herbaceous lignin, ACS Sustain. Chem. Eng. 4 (12) (2016) 6608–6617.
[44] C. Kloss, C. Goniva, A. Hager, S. Amberger, S. Pirker, Models, algorithms and validation for opensource DEM and CFD–DEM, Progr. Comput. Fluid Dyn.Int. J. 12 (2–3) (2012) 140–152.
[45] Y. Sheng, C. Lawrence, B. Briscoe, C. Thornton, Numerical studies of uniaxial powder compaction process by 3D DEM, Eng. Comput. 21 (2/3/4) (2004) 304–317.
[46] K. Ahnert, M. Mulansky, Odeint–solving ordinary differential equations in C++, in: AIP Conference Proceedings, 1389, AIP, 2011, pp. 1586–1589.
[47] E. Ranzi, A. Cuoci, T. Faravelli, A. Frassoldati, G. Migliavacca, S. Pierucci, S. Sommariva, Chemical kinetics of biomass pyrolysis, Energy Fuels 22 (6) (2008) 4292–4300.
[48] I. Milosavljevic, E.M. Suuberg, Cellulose thermal decomposition kinetics: global mass loss kinetics, Ind. Eng. Chem. Res. 34 (4) (1995) 1081–1091.
[49] P.T. Williams, S. Besler, The influence of temperature and heating rate on the slow pyrolysis of biomass, Renew. Energy 7 (3) (1996) 233–250.
[50] M. Garcia-Perez, A. Chaala, H. Pakdel, D. Kretschmer, C. Roy, Vacuum pyrolysis of softwood and hardwood biomass: comparison between product yields and bio-oil properties, J. Analyt. Appl. Pyrolysis 78 (1) (2007) 104–116.
[51] H. Yang, R. Yan, H. Chen, D.H. Lee, C. Zheng, Characteristics of hemicellulose, cellulose and lignin pyrolysis, Fuel 86 (12) (2007) 1781–1788.
[52] F. Qi, M. Wright, A novel optimization approach to estimating kinetic parameters of the enzymatic hydrolysis of corn stover, AIMS Energy 4 (1) (2016) 52–67.
[53] S. Sunphorka, B. Chalermsinsuwan, P. Piumsomboon, Artificial neural network model for the prediction of kinetic parameters of biomass pyrolysis from its constituents, Fuel 193 (2017) 142–158.
[54] M. Aghbashlo, M. Tabatabaei, M.H. Nadian, V. Davoodnia, S. Soltanian, Prognostication of lignocellulosic biomass pyrolysis behavior using ANFIS model tuned by PSO algorithm, Fuel 253 (2019) 189–198.